Chapter 15

'Universal' Synthesis of PZT (1-X)/X Submicrometric Structures Using Highly Stable Colloidal Dispersions: A Bottom-Up Approach

A. Suárez-Gómez, J.M. Saniger-Blesa and
F. Calderón-Piñar

Additional information is available at the end of the chapter

http://dx.doi.org/10.5772/51996

1. Introduction

The synthesis of nanostructured ferroelectric materials has been a subject of increasing interest for more than a decade due to their possible applications as nonvolatile/dynamic random access memories (NVRAMs/DRAMs), tunnel effect capacitors for high frequency microwave applications, infrared detectors, micro-electromechanical systems (MEMs) and electro-optical modulators among others. These materials, when fully integrated into appropriately designed micro-systems, are promising candidates for robotics sensing and for future medical procedures requiring an in situ, real time and nondestructive monitoring with very high sensitivity.

As a logical consequence, the quest for nanostructured ferroelectric materials has also led to modify the synthesis routes usually considered for obtaining conventional bulk materials and thin films. One of those routes, the sol–gel method, overcomes the inherent limitations of the conventional powders-based synthesis routes when dealing with molecular homogeneity and, therefore, it has been extensively studied and applied in different scenarios in order to obtain not only thin films, nanotubes or nanorods, but also submicron grains due to the distinctive dielectric and ferro/piezoelectric features that are associated with size related effects when average grain size is well below 1 μm [1]-[5]and because of the potential use of these materials in a plethora of nanodevices [6].

One of the backbones of the ferroelectrics industry is the Lead zirconate titanate [PZT: $Pb(Zr_{1-x}Ti_x)O_3$] ceramic system, a well-known ABO_3 perovskite with a wide range of industrial applications since the early 1950s of the 20th century. Its dielectric and electromechanical properties have made possible to develop and implement a myriad of devices such as under-

water sonar systems, sensors, actuators, accelerometers, ultrasonic equipment, imaging devices, microphones and multiple active and passive damping systems for the car industry.

The sol–gel synthesis of PZT ceramics has evolved a lot since it was first reported in the mid-1980s of the last century [7]-[9]; thermal treatments, precursors, additives, diluents and stabilizers have been incorporated and/or modified in order to achieve less hydrolysable, more stable, compounds to suit a specific need. In the case of the synthesis of thin films, nanotubes or nanorods, sol–gel routes have been used in many different ways: from the well-known spin-coating method to the electrophoretic deposition on a given substrate [10] or the insertion on nanoporous templates [11]. Submicron and nanosized PZT particles are also important in the fabrication of highly dense bulk ceramics which, even nowadays, comprise almost the entirety of the electroceramics market. In this particular case, several works have been published in which PZT powders are synthesized first via sol–gel and then put to sinter for densification [12]-[15]. In this procedure, sintering temperatures tend to lower and densification attains notably high values mostly due to a higher Gibb's free energy per unit surface area while some material properties strongly dependent on grain size are also enhanced [16].

Accordingly, in this chapter we will be devoted to analyze the feasibility of a 'customized' synthesis of $PbZr_{1-x}Ti_xO_3$ [PZT (1-x)/x] nano/submicrometric structures by using a sol-gel based colloidal dispersion as a precursor solution. This study will be done on the basis of a 'bottom-up' approach as it will take into account (i) Synthesis route, (ii) Properties of colloidal dispersions and (iii) Final crystallization. We will try to thoroughly illustrate every synthesis step while paying special attention to the physicochemical depiction of some phenomena that not always are sufficiently described or explained. It has to be pointed out that most of the main procedures, discussions and results contained herein could be easily extrapolated to a wide range of materials, not exclusively PZT-based ones.

2. Sol-gel based synthesis route

The complexity of the intermediate reactions, one of the few handicaps of the sol–gel method, makes almost mandatory a step by step study of the synthesis method. The chemical reactivity of precursors is a well-known key feature determining the nature of the intermediate organic ligands and the control of the hydrolysis rate in the final sol–gel. Several studies have been made for particular synthesis routes both theoretical and experimental and many possible reaction pathways have been proposed and dissected. Particularly, the -chemistry of metal alkoxides has been intensively studied by Sanchez et al. [17] and Sayer and coworker [18]. It is our purpose here to analyze the different reaction steps and intermediates involved in the PZT (1-x)/x sol–gel synthesis using propoxides as starting metal alkoxides.

2.1. Synthesis

The followed sol-gel route was the acetic acid, acetylacetone and 2-methoxyethanol propoxy-based sol-gel method as illustrated in Figure 1. Starting reagents for the sol-gel PZT (1-

http://dx.doi.org/10.5772/51996

x)/x solutions were: (1) lead(II) acetate trihydrate ($Pb(OAc)_2 \bullet 3H_2O$, Mallinckrodt Baker, Inc., 99.8% pure), (2) glacial acetic acid (HOAc, Mallinckrodt Baker, Inc., 99.7% pure), (3) acetylacetone (AcacH, Sigma-Aldrich Co., 99% pure), (4) 2-methoxyethanol (2-MOE, Mallinckrodt Baker, Inc., 100% pure), (5) zirconium(IV) propoxide ($Zr(OPr)_4$, Sigma-Aldrich Co., 70 wt.% in 1-propanol), and (6) titanium(IV) propoxide ($Ti(O^iPr)_4$, Sigma-Aldrich Co., 97% pure).

First, lead acetate was dissolved in acetic acid with a 1:3 molar ratio while stirred and refluxed at 115 °C during 3 h for dehydration and homogeneity purposes. After this step, a thick transparent solution was obtained which will be referred hereafter as solution A. On a separate process, stoichiometric amounts of zirconium and titanium propoxides were mixed with acetylacetone on a 1:2 molar ratio in order to avoid fast hydrolysis of reactants. This mixture was stirred and refluxed at 90 °C during 4 h forming a clear yellow solution referred hereafter as solution B. When this solution cooled down, the precipitation of several needle shaped crystals was verified. In order to keep stoichiometry unaffected, we then repeated the solution B procedure to isolate and characterize some of those crystals by single crystal XRD.

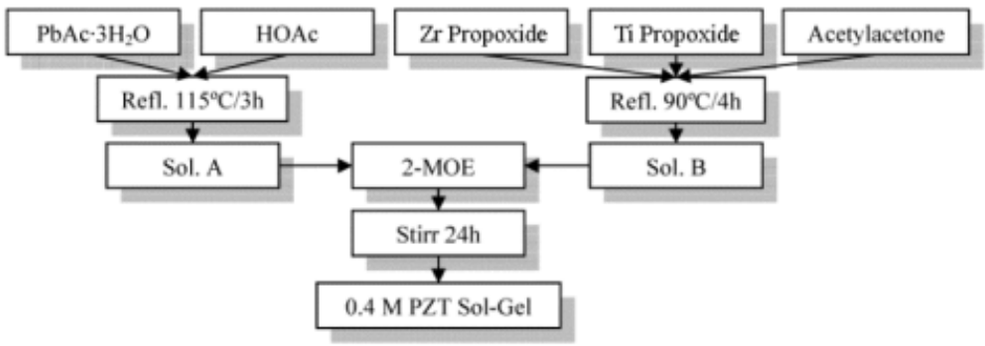

Figure 1. Flow chart depicting the basic experimental procedure followed in order to obtain a 0.4M PZT (1-x)/x sol–gel based precursor.

Solutions A and B were then mixed together as appropriate amounts of solvent (2-MOE) were slowly added for complete dilution of the precipitated crystals and for controlling the PZT concentration on the final solution. Afterwards, a light yellow solution was obtained after stirring for 24 h at room temperature.

It must be stated here that we devoted our work to several Zr:Ti molar ratios that are commonly used in practical applications: *(i)* PZT 25/75, *(ii)* PZT 53/47, *(iii)* PZT 60/40, *(iv)* PZT 80/20 and *(v)* PZT 95/05. Besides, we also tried to cover a relatively wide concentration range for every PZT (1-x)/x sol-gel precursor under study: from 0.05 M to 0.4 M. Due to these facts, we will only focus on the discussion of representative samples instead of discussing irrelevant data of samples that showed no significant discrepancies between each other. As depicted in Figure 1, this section will analyze the synthesis of a 0.4 M PZT 53/47 precursor solution.

2.2. Experimental techniques

Every reactant and intermediate product was analyzed using FT-IR and Raman spectroscopies. As was described earlier, single crystal XRD was also carried out for the solution B acicular precipitates.

2.2.1. Raman spectroscopy

Raman characterization was made on an Almega XR Dispersive Raman spectrometer equipped with an Olympus microscope (BX51). An Olympus 10x objective (N.A. = 0.25) was used both for focusing the laser on the sample, with a spot size ~ 5 μm, and collecting the scattered light in a 180° backscattering configuration. The scattered light was detected by a CCD detector, thermoelectrically cooled to -50 °C. The spectrometer used a grating (675 lines/mm) to resolve the scattered radiation and a notch filter to block the Rayleigh light. The pinhole of the monochromator was set at 25μm. The Raman spectra were accumulated over 25 s with a resolution of ~ 4 cm^{-1} in the 100-2000 cm^{-1} interval. The excitation source was a 532 nm radiation from a Nd:YVO_4 laser (frequency-doubled) and the incident power at the sample was of ~ 8 mW.

2.2.2. FT-IR spectroscopy

FT-IR analysis was carried out on a Thermo Nicolet Nexus 670 FT-IR in transmission mode with a resolution of ~ 4 cm^{-1} in the 400-2000 cm^{-1} interval. The excitation source was a Helium-Neon laser light incident on a KBr compact target containing ~ 0.5 % in weight of the sample of interest.

2.2.3. Single crystal XRD

Single crystal XRD experiments were carried out for selected specimens. A Bruker SMART APEX CCD-based X-ray three circle diffractometer was employed for crystal screening, unit cell determination and data collection. A Van Guard 40x microscope was used to identify suitable samples and the goniometer was controlled using the SMART software suite. The X-ray radiation employed was generated from a Mo sealed X-ray tube (Kα= 0.70173 Å with a potential of 50 kV and a current of 30 mA) and filtered with a graphite monochromator in the parallel mode (175 mm collimator with 0.5mm pinholes).

2.3. Solution A

Figure 2 shows, from bottom to top, the IR and Raman spectra of starting acetic acid and lead acetate as well as the final product, solution A, after stirring and refluxing. There are several features in common between these spectra due to the organic nature of ligands. Basically, bands corresponding to the CH_2 and CH_3 groups in the 1300-1400 cm^{-1} interval as well as in the low frequency range [19].

The glacial acetic acid spectra reveal several representative peaks found at 619 cm^{-1} (RA: Raman active), 889-893 cm^{-1} (RA, IRA: Infrared active), 1294 cm^{-1} (IRA), 1410 cm^{-1} (IRA), 1668

http://dx.doi.org/10.5772/51996

cm^{-1} (RA), 1716 cm^{-1} (IRA) and 1757 cm^{-1} (IRA) for this molecule. Those peaks correspond, respectively, to the τ(C-C=O), ν(C-C), $\delta_S(CH_3)$, $\delta_A(CH_3)$, ν(C=O), $\nu(C=O)_{dimer}$ and $\nu(C=O)_{monomer}$ vibrations [20],[21]. The clear splitting detected for the C=O dimeric and monomeric stretch vibrations somewhat evidences the presence of some small amounts of water in the acidic medium that, for the purpose of our study, will not be taken into consideration.

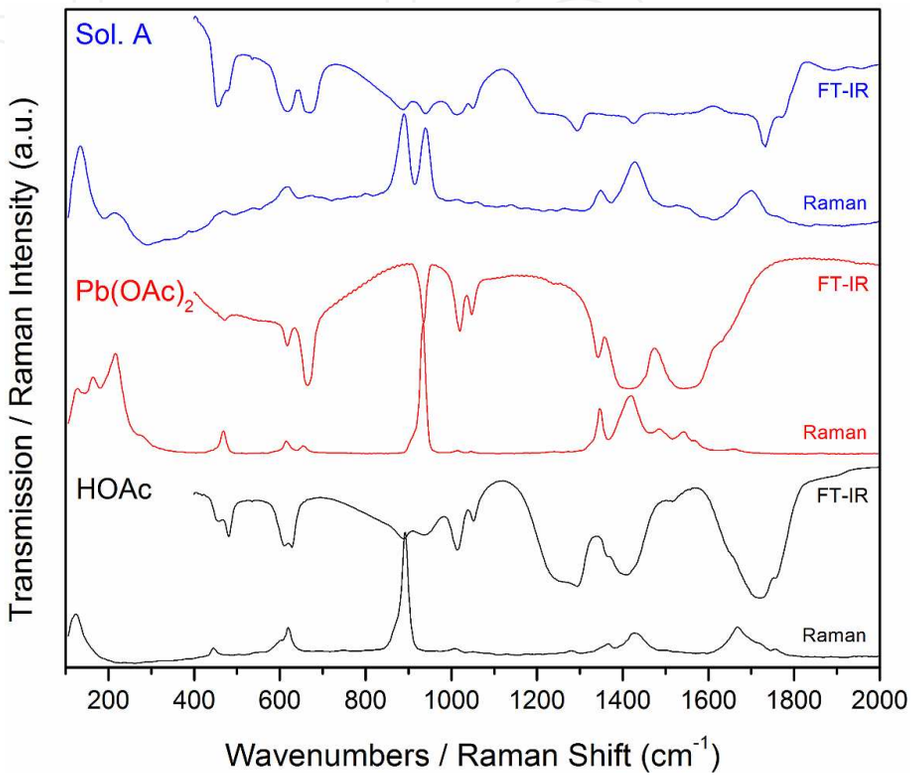

Figure 2. Infrared and Raman spectra of the reactants involved in solution A formation.

On the other hand, the lead(II) acetate trihydrate spectra also feature some representative peaks located at 216 cm^{-1} (RA), 615-617 cm^{-1} (RA, IRA), 665 cm^{-1} (IRA), 934-935 cm^{-1} (RA, IRA), 1342-1346 cm^{-1} (RA, IRA), 1417-1420 cm^{-1} (RA, IRA) and 1541-1543 cm^{-1} (RA, IRA) related to the ν(Pb-O), ϱ(COO), δ_S(COO), ν_S(C-C), $\delta_S(CH_3)$, ν_S(C-O) and ν_A(C=O) vibrational modes, respectively [20],[22]. It is well known that the acetate ligands can complex a metal ion in three different ways (monodentate, bidentate chelating and bridged) and that, unfortunately, none of these can be uniquely identified by symmetry considerations. Traditionally, the various types of bonding have been identified by the magnitude of the difference between symmetric ν_S(C-O) and asymmetric ν_A(C=O) vibrations. In our case, this difference is 122 cm^{-1} indicating a bidentate chelating coordination for the acetate-metal complex that has been widely accepted for lead(II) acetate even though the $\Delta\nu$ criterion has led sometimes to incorrect conclusions [20],[22].

Solution A vibrational spectra shown in Figure 2 evidences the expected dilution of lead(II) acetate in acetic acid: there are no new vibrational modes and a strong band overlapping is seen. There is some band shift due to the overlapping and is worth to notice the weakening

of the lead acetate Raman active Pb-O band at 216 cm^{-1} when in solution. Unfortunately, a noticeable fluorescence in the Raman spectrum could not be avoided and this fact made very difficult to carry on an appropriate analysis with useful data.

Nevertheless, and according to our results, the formation of Solution A could be fairly described by the following equation:

$$Pb(OAc)_2 \cdot 3H_2O_{(s)} + 3HOAc_{(Aq)} \xrightarrow[t\sim 3\,hrs.]{T\sim 115^{\circ}C} Pb^{2+}_{(Aq)} + 3\alpha H_3O^{+}_{(Aq)} + (2+3\alpha)OAc^{-}_{(Aq)} + \\ +3(1-\alpha)HOAc_{(Aq)} \quad (1)$$

Where α is the HOAc dissociation degree under our experimental conditions and where we have also assumed, on the simplest approach, neglectable losses due to evaporation of H_2O and HOAc during the whole process.

2.4. Solution B

FT-IR spectra for Solution B precursors, Figure 3, showed some features like the ones discussed above. A Raman spectra based analysis for these compounds could not be completed due to the strong fluorescence exhibited by the zirconium and titanium alkoxides at our fixed operating laser wavelength.

The titanium propoxide IR spectrum exhibit sharp bands at 1377-1464 cm^{-1} corresponding, respectively, to the stretching and bending vibrations of the aliphatic CH_3 groups. A distinctive single peak at 1011 cm^{-1} corresponds to the propoxy- Ti-O-C vibration and a similar behavior is found for zirconium propoxide with Zr-O-C vibrations located at 1142 cm^{-1}[18].

The acetylacetone vibrational spectrum shows the main features attributed to the most probable staggered conformation of this compound. This conformation has some typical weak IR active vibrations in the low frequency range, as it is shown. Modes at 509, 554 and 640 cm^{-1} correspond to the in plane ring deformation (Δ ring), out of plane ring deformation (Γ ring) and Δ ring + ϱ(CH_3) modes, respectively [23].

As described above, when reaction took place, some crystals precipitated short after solution B reached room temperature; IR spectra of these single crystals are also shown in Figure 3. Unlike solution A, a reaction is now verified by the shifting and/or reinforcement of bands associated to reactants vibrations. A discussion of several mechanisms for this kind of reaction has been reviewed by several authors taking into account, primarily, the mixing conditions, the reactivity of metal alkoxides and the Acac/Alkoxides molar ratio [17],[18],[24].

2.4.1. Single crystal XRD characterization

At this stage, a suitable colorless parallelepiped 0.356 mm × 0.162 mm × 0.066 mm was chosen from a representative sample of crystals of the same habit. After the determination of a suitable cell, it was refined by nonlinear least squares and Brava is lattice procedures. The unit cell was then verified by examination of the (h k l) overlays on several frames of data,

http://dx.doi.org/10.5772/51996

including zone photographs, and no super cell or erroneous reflections were observed. A search performed on the Cambridge Structural Database and updates using the program Conquest afforded 77 coincidences within 1% of the longest length of a monoclinic C-centered cell whose lattice parameters and reported structure are shown in Figure 4(a). Two entries, those with ACACZR and ZZZADD CCD reference code, in addition, revealed chemical coincidences (both in composition and stoichiometry) for the compound tetrakis(acetylacetonate-O,O')-zirconium(IV) or $Zr(Acac)_4$.

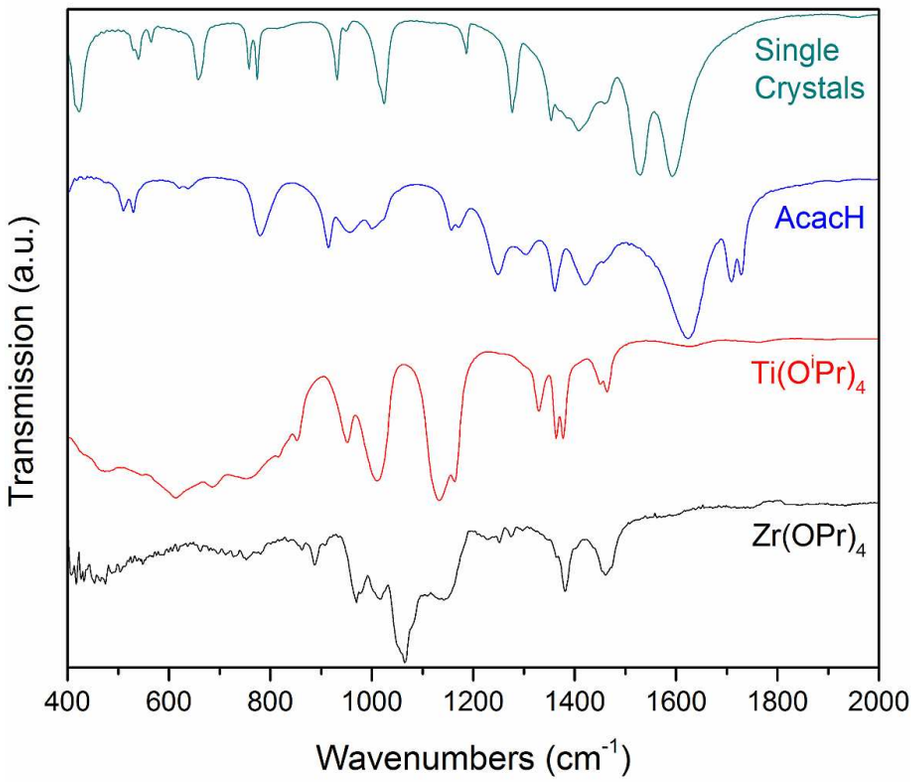

Figure 3. Infrared spectra of the reactants involved in solution B formation. The IR spectra for the resultant precipitated single crystals are also shown.

According to these data, the $Zr(Acac)_4$ structure was simulated using the Accelrys Materials Studio 3D visualizer environment [25]as shown in Figure 4(b). In this case, the acetylacetone reaction with the Zr propoxide results in the formation of an oxo cluster where the metallic atom changes its coordination number from 4 to 8 which is the highest possible value for zirconium. Metallic cations are now bonded to the acetylacetonate chelating ligand giving rise to a less hydrolysable organic complex.

In the case of the titanium propoxide reaction, and taking into account our experimental conditions, it is not a bad assumption to consider the formation of a fully chelated organometallic complex, just as it was described for zirconium. Given the maximum coordination number of 6 for titanium, a $Ti(Acac)_2(OPr)_2$ compound will be the most likely to expect as is also confirmed by earlier reports that consider the multiple chelation routes for titanium

propoxide [18],[20]. Figure 4(c) shows a very simple Materials Studio 3D modeling for the most probable configuration of $Ti(Acac)_2(OPr)_2$ as determined by the Forcite package [25] on a single step relaxation and energy minimization routine.

Accordingly, bands located at 1280, 1370-1440 and 1530-1595 cm^{-1} in the crystals spectrum, shown in Figure 3, can be assigned to the ν(C-CH_3:Acac), δ(CH_3:Acac) and ν(C-C) + ν(C-O:Acac) vibrational modes, respectively [26].

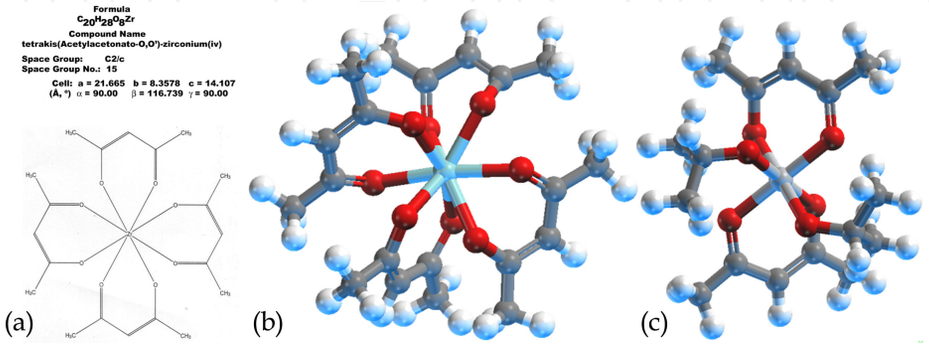

Figure 4. Fully chelated metal-acetylacetonate complexes. (a) $Zr(Acac)_4$ as reported by single crystal XRD charaterization, (b) $Zr(Acac)_4$ structure simulated by Materials Studio (MS) according to its crystallographic data and (c) $Ti(Acac)_2(OPr)_2$ simulated by MS according to its most probable configuration.

2.4.2. Chemical reaction

As seen before, solution B can be thought as the resulting chelated metal complexes mixed with residual isopropanol. In this case, an appropriate chemical equation for the reaction could be:

$$\begin{aligned} &0.53Zr\left(O^i\,\mathrm{Pr}\right)_{4(Aq)} + 0.47Ti\left(O^i\,\mathrm{Pr}\right)_{4(Aq)} + 2AcacH_{(Aq)} \xrightarrow[t\sim 4hrs.]{T\sim 90^\circ C} 2HO^i\,\mathrm{Pr}_{(Aq)} + yZr\left(Acac\right)_{4(S)} + \\ &+\left(1-2y\right)Ti\left(Acac\right)_2\left(O^i\,\mathrm{Pr}\right)_{2(Aq)} + \left(0.53-y\right)Zr\left(O^i\,\mathrm{Pr}\right)_{4(Aq)} + \left(2y-0.53\right)Ti\left(O^i\,\mathrm{Pr}\right)_{4(Aq)} \end{aligned} \tag{2}$$

where we have assumed that all the acetylacetone reacts with the alkoxides thus forming the chelated organometallic complexes. As we see, there is still a fraction of nonchelated reactants due to the insufficient amount of acetylacetone needed for that purpose. Let us find now the exact amount of acetylacetone required for obtaining fully chelated organometallic complexes without any further byproducts. We could rewrite equation [2] as:

$$\begin{aligned} &0.53Zr\left(O^i\,\mathrm{Pr}\right)_{4(Aq)} + 0.47Ti\left(O^i\,\mathrm{Pr}\right)_{4(Aq)} + (2+\Delta)AcacH_{(Aq)} \xrightarrow[t\sim 4hrs.]{T\sim 90^\circ C} (2+\Delta)HO^i\,\mathrm{Pr}_{(Aq)} + \\ &+0.53Zr\left(Acac\right)_{4(S)} + 0.47Ti\left(Acac\right)_2\left(O^i\,\mathrm{Pr}\right)_{2(Aq)} \end{aligned} \tag{3}$$

http://dx.doi.org/10.5772/51996

Now, it is obvious that Δ = 1.06 implying an alkoxides: acacH molar ratio of 1:3.06 for full chelation of metallic centers. Equation [3] can now be written for any given Zr:Ti ratio (1-x)/x:

$$(1-x)Zr\left(O^{i}\,\mathrm{Pr}\right)_{4(Aq)} + xTi\left(O^{i}\,\mathrm{Pr}\right)_{4(Aq)} + 2(2-x)AcacH_{(Aq)} \xrightarrow[t\sim 4hrs.]{T\sim 90^{\circ}C} 2(2-x)HO^{i}\,\mathrm{Pr}_{(Aq)} + \\ +(1-x)Zr\left(Acac\right)_{4(S)} + xTi\left(Acac\right)_{2}\left(O^{i}\,\mathrm{Pr}\right)_{2(Aq)} \tag{4}$$

This equation represents an extension for the initially proposed sol-gel based route in order to obtain fully chelated and no hydrolysable precursor solutions for PZT based ferroelectric materials. It allows us to synthesize PZT at any Zr:Ti ratio while maximizing solution stability and offering a noticeable repetitiveness for both small and large scale manufacturing and processing.

On the following section we will analyze some features of different sol-gel based PZT (1-x)/x precursors when synthesized using the universal 1:2(2-x) alkoxides: acacH molar ratio already discussed above.

3. Some properties of the PZT precursors

In the final step of the synthesis, when mixing Solutions A and B with 2-methoxyethanol, the dissolved lead acetate complex can react with 2-MOE forming a very stable acetate–methoxyethoxy lead complex [27] that, along with the chelated metal complexes already formed, may lead to turn this final solution into a hydrophobic sol, poorly hydrolysable and, therefore, very stable.

Stability issues tend to be crucial when using sol-gel based precursors in research, small scale applications and industry. Therefore, it is very important to keep control over some parameters that affects the solution stability and, most of all, the average particles size. Particularly, particles size can be an indicator of some undesirable processes that could be taking place in the sol: aggregation, flocculation and sedimentation; aggregation, even though is a reversible process, is a good indicator of instability since the other two processes, which are not reversible, generally follows after some time.

In this respect, the aging time dependences of some physical parameters directly related to the stability of colloidal dispersions must be explored and discussed. Two of the most important parameters that should be taken into account are pH and the average particles size. The first one is determinant for fixing the thickness of the ionic layers surrounding any given charged colloidal particle (Stern layers) while affecting, at the same time, the Zeta potential, the electrophoretic mobility and the aggregation mechanisms as well as the apparent hydrodynamic particle size. As a consequence, the average particles size is the final result of the conjugate action of all the physicochemical variables hardly mentioned before. It is also the definitive experimental variable on which any post processing technique should be

based on as it explicitly defines the size range of the so called "building blocks" for bottom-up studies or applications.

Currently, there are no known extensive reports in the literature directly concerned to the study of the time dependence of the average particles size or pH in a PZT precursor sol. It must be noted that, in the case of magnetic nanoparticles, some studies have been carried out [28]-[30]and all of them stress the strong correlation between the size of the colloidal particle and the final properties of the conceived structure, whether it will be nano- or not.

3.1. pH

For this study, we synthesized PZT (1-x)/x precursor solutions by using the same route described in 2.1 with the only difference being the propoxides: acacH molar ratio. In this case, and for the rest of our text, that ratio will be 1:2(2-x) for full chelation of the metal alkoxides.

As it was stated earlier, we will avoid again showing and discussing irrelevant data of samples that showed no significant discrepancies between each other and, because of this, this section will analyze the pH vs. Concentration vs. aging time behaviors of several PZT 53/47 precursor solutions with concentrations ranging from 0.05 M to 0.37 M in a time interval of up to 4 months of stocking.

As can be seen in Figure 5, the acidity/basicity of the solutions clearly shows a tendency with both sols concentration and aging time. Figure 5(a) shows the measured pH vs concentration for the studied sols at several aging steps and, as expected, the more concentrated sample implies the more acidic medium which is consistent with the chemical reaction proposed for sols synthesis.

Figure 5(b), on the other hand, shows the measured pH vs. time behavior. As a general tendency, sols pH dependency with aging time can be divided in three stages which are highlighted in the graph: (i) pH increases notably in the first days after which (ii) it decreases to values somehow close to the initial ones. In this moment, (iii) pH starts to rise again but with a slower time gradient than on stage (i). In our opinion, for the understanding of the pH vs. aging time behavior, we have to take into account the coexistence of different competitive processes right after sols were prepared. In this way, a qualitative description could be done as follows [31]: (i) Remnant unreacted acetic acid evaporates during the first days implying a decrement on the acidity of sols. At this point, (ii) particles are less positively charged and are able to aggregate via condensation reactions followed by the formation of small portions of alcohol (1-propanol) and thus implying a more acidic environment as seen in Figure 5. The number of polyanions per aggregate chain must be limited, however, by the high chemical stability of the chelated metal complexes and that is why the aggregation process does not imply polymerization and/or gelation as it has been reported for more hydrophilic sols. Shortly after condensation rate vanishes, (iii) it is possible for the residual alcohols to evaporate as solutions age thus allowing pH to rise slowly, as seen in Figure 5 for the more aged solutions.

At this scenario, however, hydrolysis is not expected due to (a) the complete chelation of the metal complexes, (b) to the short lengths of the already formed polymeric chains and, there-

http://dx.doi.org/10.5772/51996

fore, (c) to the small amount of alcohol that could be formed afterwards. After 4 months of aging, no noticeable changes in pH values were detected. Moreover, the stability of these solutions could be eye inspected by verifying neither the absence of sedimentation nor precipitation of single particles or aggregates after almost 1 year of stocking.

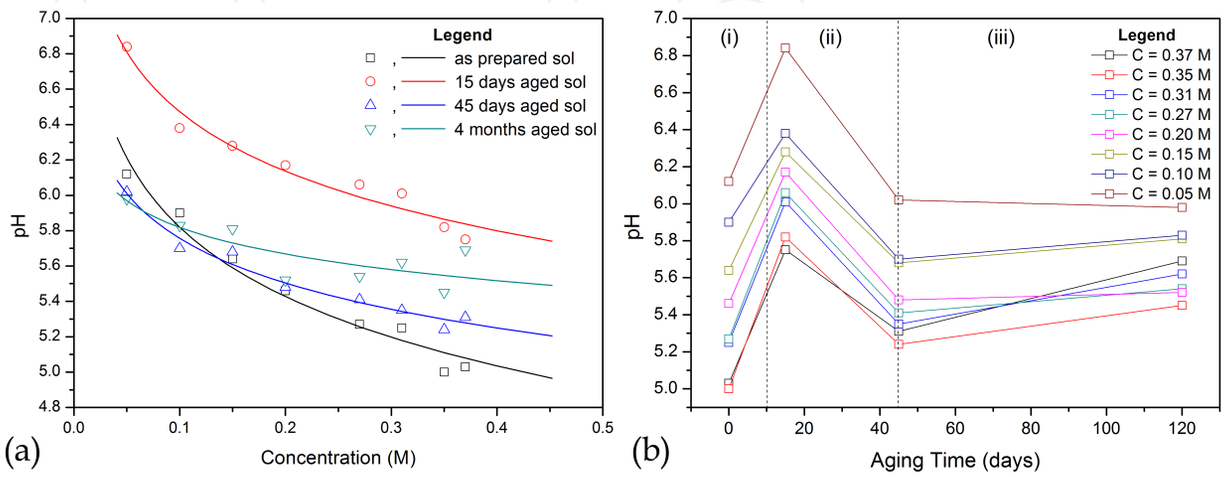

Figure 5. a) pH vs. concentration dependencies for the PZT 53/47 samples understudy measured at different time intervals. Semi-log fittings to guide the eye are also drawn. (b) Aging effects on pH for the same samples. Three distinctive stages were detected and are highlighted in the graph.

3.2. Mean particle size

3.2.1. Experimental technique

Particles size measurements were carried out by means of the dynamic light scattering (DLS) technique in a Zetasizer Nano ZS90 manufactured by Malvern Instruments Ltd. equipped with a HeNe laser source. Approximately 1.5 ml of as synthesized sols were stored in polystyrene cells (DTS0012 cells) provided by the same manufacturer and then size distributions curves were recorded from the very first day until 125 days after synthesis. For this purpose, several solvent parameters were needed for further processing of dispersed light intensity, namely viscosity ($\eta_{2\text{-MOE}}$ ~ 1.5410 cP), dielectric constant ($\varepsilon_{2\text{-MOE}}$ ~ 16.9) and refraction index ($n_{2\text{-MOE}}$ ~ 1.33) [32]. After each measurement, a nonlinear least squares fitting (NLLSF) was made to the experimental data according to a log-normal distribution function:

$$f_{\ln}(x,\beta_i) = \beta_0 + \frac{\beta_1}{\sqrt{\pi}\beta_2}\frac{1}{x}\exp\left[-\frac{1}{2\beta_2^2}\ln\left(\frac{x}{\beta_3}\right)^2\right] \quad (5)$$

Where β_i are fitting parameters. It must be stressed that this fitting was carried out only for size intervals where unimodal distribution curves were measured.

3.2.2. Concentration dependence

Figure 6 shows the results obtained for particles size distribution for two concentrations under study (a PZT 53/47 precursor) after different time lapses that are also shown in the figure.

According to what is shown, an appropriate discussion relaying on the acidity/particles size dependence cannot be easily established: oscillations in the pH values, see Figure 5, during aging are not followed by oscillations in the mean particles size values. Even though this feature is not fully understood, it may be due to the short lengths of the oligomeric chains present in the solution and to the weak sensitivity of the completely chelated metal complexes to the ionic strength of the solvent medium. Another possible explanation could be given in terms of the irreversibility associated to the formation of these chains when the solvent medium is not acidic enough to break the corresponding bonds and/or coordinations.

As can be seen, as prepared sols featured multimodal distributions with some small percent of particles that could even have sizes higher than 1μm. As solutions are aged, these distributions tend to be unimodal featuring a mean particles size well below 10 nm. We consider that this is a remarkable result of this work as it shows that there is no rule of thumb closely related to the need of using fresh, as prepared solutions for synthesizing several kinds of nanodimensional systems by means of electrophoretic deposition(EPD) or simple template immersion, [33]-[36]. Moreover, in this case we could have chosen solutions aged for 20 days or more for bulk, thin films or nanostructures synthesis due to the better homogeneity regarding particles size distribution in both cases under study.

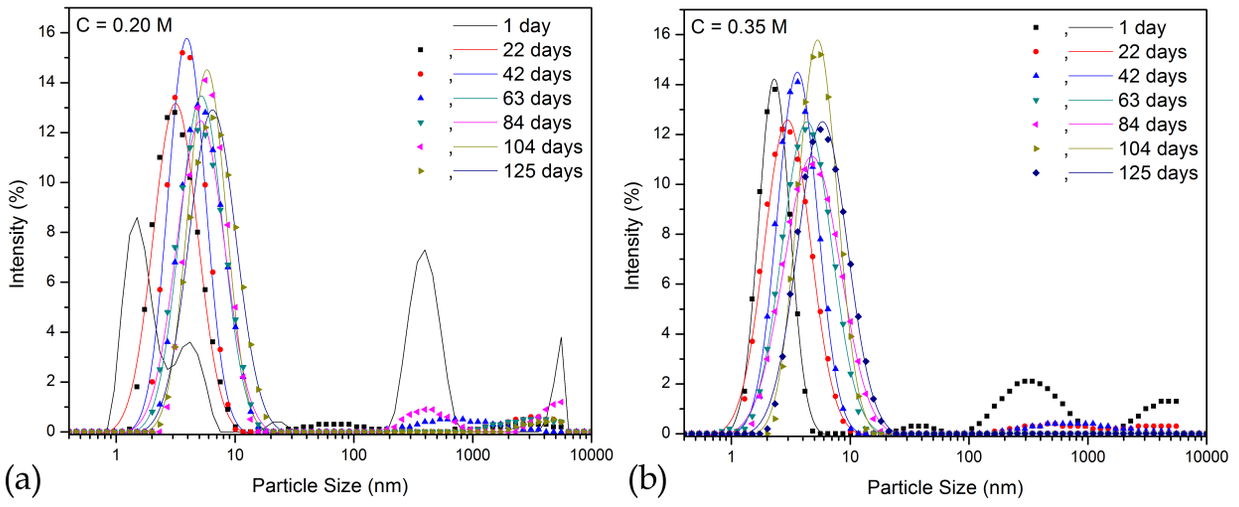

Figure 6. Particles size distribution functions for the analysed PZT 53/47 precursor solutions and for several aging times in the whole measurement range. Log-normal fittings for the more populated size intervals are also depicted.

This behavior could be explained, in principle, on the basis of the chemical reaction which was described for obtaining what we called solution B, see Section 2.4. As we stated, by the end of this step we observed the crystallization of the compound $Zr(Acac)_4$. Such crystallization does not occur after mixing solutions A and B in the presence of 2-MOE which can be attributed (I) to the higher acidity of the final A+B+2-MOE solution, (II) to the solubility of

$Zr(Acac)_4$ in 2-MOE, (III) to a dilution process while mixing A+ B, or (IV) to a combined effect of all of the above. Must be noted that the less acidic solution (C = 0.20M) possesses, at the same time, the less unimodal distribution function which is an expected result in concordance to the relationship between ionic strength and particles size.

Thus, it seems plausible to assume solution B as a dispersion containing the $Ti(Acac)_2(OPr)_2$ compound at molecular level and submicrometric aggregates of $Zr(Acac)_4$ that do not precipitate; these are redissolved afterwards when mixed with the acetate rich solution A and 2-MOE. After stirring the resultant sol for one day, the size of some percentage of the $Zr(Acac)_4$ aggregates still ranges between 100 and 1000 nm; after 20 days, however, size is well below 10 nm. From these results, and somehow confirming our previous discussion, we can also see that the less concentrated solution features a considerable amount of particles with sizes well above 50nm even after 100 days of stocking. For this reason, we will focus our attention from now on in precursor solutions with 0.35 M aged during the first 30-35 days, a time period that, according to our results, seems to be critical in the colloidal stability of as synthesized sols.

3.2.3. Aging time dependence

As it was said before, all samples under study featured a noticeable stabilization when aged for about 1 month. Figure 7 shows this aging behavior for two PZT (1-x)/x precursor solutions concentrated at 0.35 M. In all cases, it could be observed a similar time evolution as the one described earlier for Figure 6.

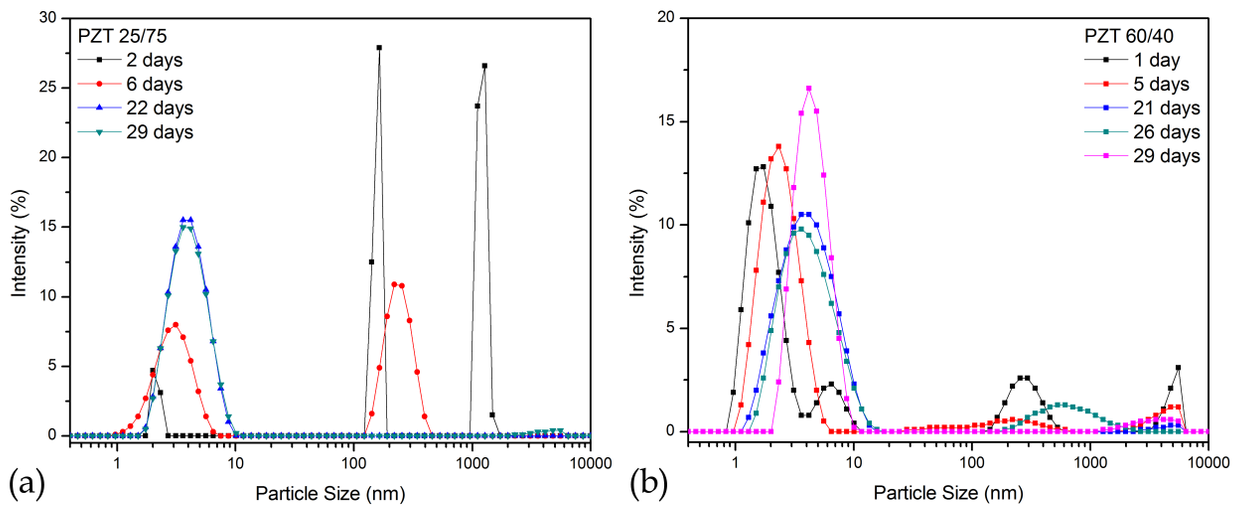

Figure 7. Aging behavior, as depicted by the time evolution of particles size distribution curves, for two PZT (1-x)/x precursor solutions concentrated at 0.35 M: (a) PZT 25/75 and (b) PZT 60/40.

On the other hand, Figure 8 shows the whole dataset of the measured mean particles size for the synthesized solutions. Fitting curves shown here were determined by considering a time dependence given by $\langle d \rangle = C_1 t^{1/(1-\lambda)} + C_2$ that, according to the classical Smoluchowski theory in the van Dongen–Ernst approximation, describes appropriately a nongelling system of dis-

persed clusters. Moreover, in the same approximation, the small values of $\lambda(\lambda<<1)$ are usually associated with a Brownian diffusion limited aggregation process vastly dominated by collisions between larger clusters with smaller ones [31].

Another view of the aging process could be illustrated by means of the dimensionless normalized distribution curves, not shown here. In that representation, the broadening of the distribution curves with aging is an indicator of very likely aggregation processes and somehow will help to complete the kinetic analysis that we have been through in this section.

In a way of summarizing our results, it could be said that, just after synthesis, several populations of particles were detected until homogenized a few days later; then particles tend to grow very slowly with time according to an almost linear law (corresponding to that describing a nongelling system) and aggregation is expected. Moreover, these cases fit very well in the Brownian diffusion limited aggregation type where smaller clusters stick to bigger ones when they collide. The slow but evident increase in the mean cluster size, as well as the noticeable broadening in the distribution peaks, must warn us about an undesirable and irreversible precipitation process for, hypothetically, $t \rightarrow \infty$.

The high stability shown by our samples even after 4months of stocking and the small values for mean particles size (well below 10 nm) are good indicators that the complete chelation of the organometallic compounds plays a key role in keeping short, and poorly reactive, oligomeric chains. An aggregation process dominated exclusively by Brownian motion is highly desirable when solution stability needs to be maximized.

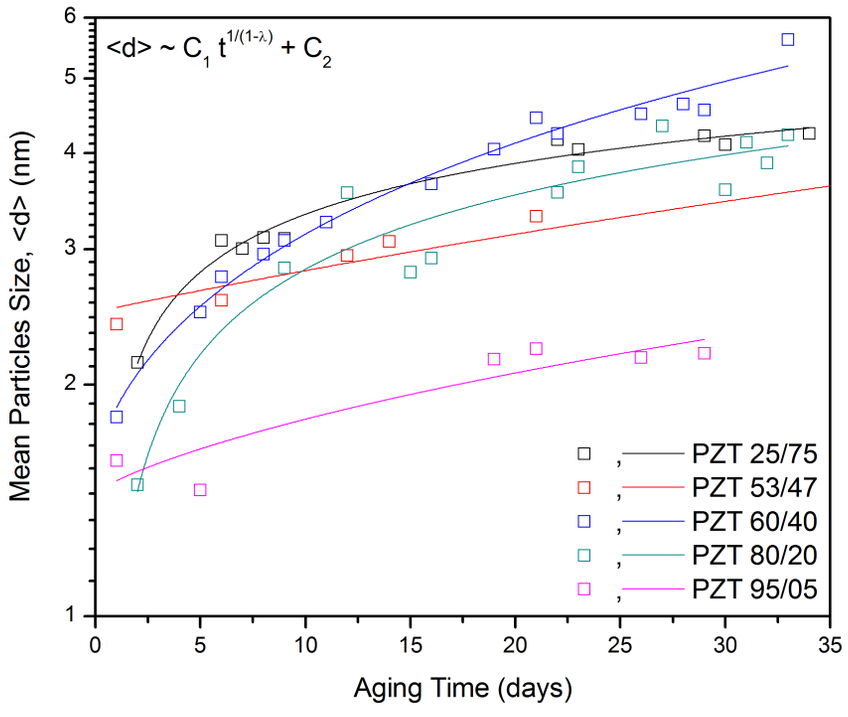

Figure 8. Mean particles size vs. aging time dependence for the systems under study. Fitting curves obeying a $t^{1/(1-\lambda)}$ scaling law are depicted.

http://dx.doi.org/10.5772/51996

Our samples were also characterized by the High Resolution Transmission Electron Microscopy (HR-TEM) technique. A few drops of the synthesized sols were deposited on copper grids, evaporated afterwards and put under a JEOL JEM2200 microscope with Omega filter and a spherical aberration corrector; some of the obtained images are shown in Figure 9 for a PZT 95/05 precursor solution. As expected, particles are likely to coalesce as the solvent evaporated prior to characterization, see Figure 9(a) and (b), and some of those nanoparticles are shown in higher magnification images in Figure 9(c) and (d). Most of the features regarding particle size that were discussed earlier were corroborated by means of this technique for all the precursor solutions.

At this point, and considering what has been discussed until now, it must be highlighted that a rigorous control of the chelation rate, pH and aging time could give us a chance to "tune" the average nanoparticles size and/or the colloidal stability as desired. By looking back at Figure 5 through Figure 8 one may feel free to choose to explore several "working points" according to our research or technological needs for every (1-x)/x Zr:Ti ratio in the PZT system.

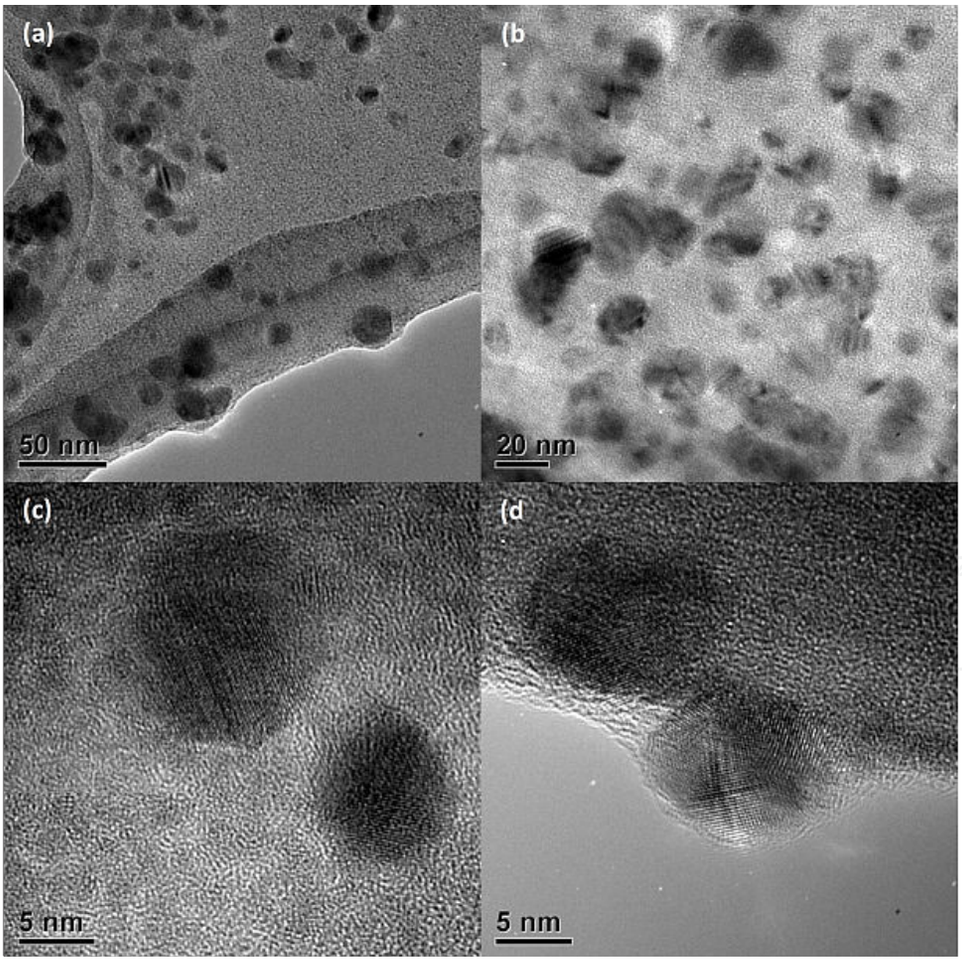

Figure 9. HR-TEMimages at different magnifications for a PZT 95/05 precursor solution, with C = 0.35 M and aged for 2 months.

This, in fact, is a powerful tool provided by the physicochemical phenomena and mechanisms previously discussed and, generally speaking, could be extended to other material systems of technological interest at a moderate cost.

4. Crystallization route

The final A + B + 2-MOE solutions were dried at 100°C for several days and, after that, they were thermally treated in order to analyze the phase evolution from the amorphous PZT sol-gel network to the expected final Perovskite structure. Due to fundamental similarities among the different samples we will be discussing only the case where Zr:Ti ratio is 53/47, concentrated at 0.35 M and aged for 2 months.

4.1. Experimental techniques

Crystallization was monitored by means of FT-IR and Raman vibrational spectroscopies, see Sections 2.2.1 and 2.2.2, and by X-Ray Diffraction (XRD) and Scanning Electron Microscopy (SEM) techniques after treating the samples for 12 hours at certain temperatures that were previously chosen. For the sake of clarity, we decided to divide the crystallization study in two temperature intervals: (i) $100 \leq T \leq 510^{\circ}C$ and (ii) $550 \leq T \leq 900^{\circ}C$. At this point, it is important to say that, for powders heated at 850°C and 900°C, the treatment was carried out for just 2 hours due to the high volatility of lead for 850°C and beyond.

Scanning Electron Microscopy (SEM) was carried out on fine ground powders in a Leica Cambridge Stereoscan 440 microscope and the X-Ray powder diffraction patterns were recorded over a 20-60° 2θ range on a Bruker D8 Advance diffractometer with filtered CuKα radiation. In this technique, the identified phases were indexed by comparing the resulting diffraction patterns with those of similar compositions reported in the International Union of Crystallography (IUCr) JCPDS-ICDD database.

4.2. 100 ≤ T ≤ 510 °C

In this temperature range the material goes through very noticeable phase transformations; the initial amorphous powder starts to show some crystallinity for about 500°C, right after the combustion of the remaining organic species. Figure 10 shows these first crystallization stages as recorded by the Raman (a) and FT-IR (b) vibrational spectroscopies. The vibrational modes associated to the remnant organic compounds coexisting after heat treating at 100 °C are also highlighted in this graph, Figure 10(b), and it must be noticed that they correspond, basically, to the lead acetate and to the completely chelated organometallic complexes. More explicitly, numbered modes in Figure 2(b) have been assigned to: (1)$Pb(OAc)_2$:ϱ(COO), (2)$Pb(OAc)_2$:δ_S(COO), (3)$Pb(OAc)_2$:ν_S(C-C), (4)$Ti(OPr)_2(Acac)_2$:Ti-Acac, (5)$Zr(Acac)_4$:Zr-Acac,(6)$Pb(OAc)_2$:$\delta_S(CH_3)$, (7)$Ti(OPr)_2(Acac)_2/Zr(Acac)_4$:$\delta(CH_3$:Acac) + $Pb(OAc)_2$:ν_S(CO)and (8)$Ti(OPr)_2(Acac)_2/Zr(Acac)_4$:[ν(C-C) + ν(C-O:Acac)] + $Pb(OAc)_2$:ν_A(C=O)[26],[37].

http://dx.doi.org/10.5772/51996

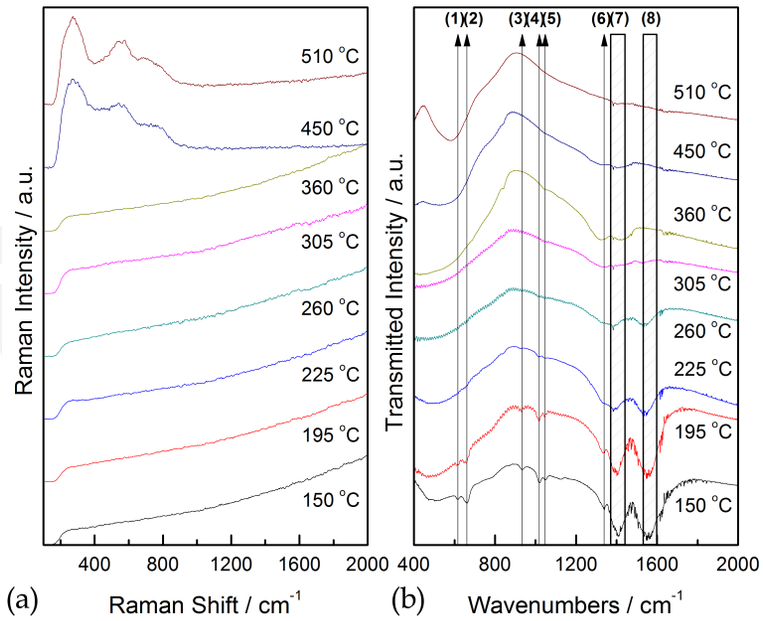

Figure 10. Phase transformations for 100 °C≤ T≤ 510 °C as registered by Raman (a) and FT-IR (b) vibrational spectroscopies; in this case, remnant vibrations due to the presence of acetate and chelated metal complexes are highlighted.

Until 225˚C, IR spectra showed no variation; the intensity ratios between the detected modes are almost the same and, on the other hand, Raman spectra featured no signal given the strong presence of π-bonded organic species. Afterwards, IR spectra revealed the almost complete decomposition of acetates and a decrement of Metal:Acac complexes while any noticeable Raman signal is still absent. Just after T = 450˚C the active Raman modes normally assigned to a PZT 53/47 started to show up. After treating at this temperature, the FT-IR spectra reveals the formation and definition of the A1(3TO) vibrational mode (~600 cm^{-1}) which is also characteristic for this compound [38]-[41].

Another view of the whole process in this temperature range could be given, as seen in Figure 11, by means of XRD characterization. XRD patterns clearly illustrate the phase transformation exhibited by an amorphous material turning into crystalline; as for the Raman spectra, crystallinity starts to get noticed at T = 450˚C. However, these patterns revealed the existence of well defined peaks near 28˚ that disappear almost entirely at 510°C.

These maxima are usually associated to an intermediate metastable phase belonging to the Fluorite crystal system (F) which is mainly characterized by the spatial disarrangement of the oxygen atoms, vacancies and metal cations while coexisting with some carbonates and/or oxides that still remain in the material. Afterwards, when carbonates and oxides react, a new metastable phase is formed but this new arrangement tends to be more ordered than the previous fluorite. This intermediate phase is considered as belonging to the Pyrochlore crystal system (P or Pyr) and consisting of a 2 x 2 x 2 ordered fluorite cell with oxygen and metallic vacancies or, from another point of view, consisting of a 2 x 2 x 2 non stoichiometric Perovskite (Per) cell. This rigorous differentiation between Fluorite and Pyrochlore is not always considered in literature and it can be subtle sometimes, especially when working

with a well known compound as PZT is. Anyway, in Figure 11 we have denoted by F (Fluorite) and P (Pyrochlore) the diffraction maxima associated with each of these phases and according to the indexed cubic structures reported in reference [42] (a = 5.25 Å) and in reference [43] (a = 10.48Å), respectively.

Up to this point, we have seen the almost complete elimination of organic ligands with heating as well as the amorphous/crystalline phase transformation going through two intermediate metastable phases. In the next subsection we will carry on a similar study for higher temperatures while exploring the formation of pure Perovskite phase with morphological quality.

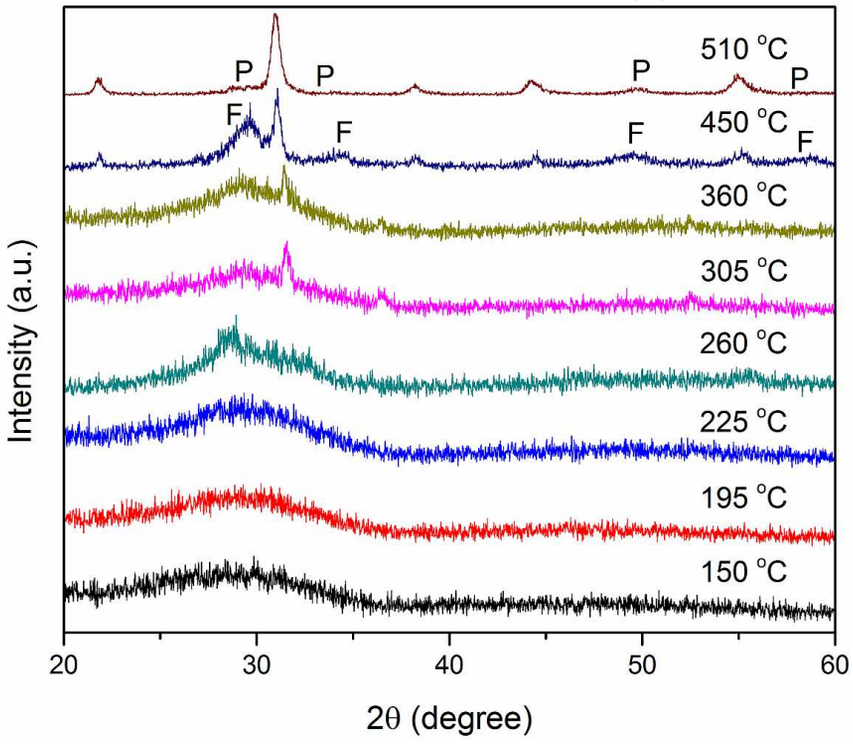

Figure 11. Thermal evolution of PZT 53/47 precursor powders when100 °C≤ T≤ 510 °C as recorded by XRD patterns.

4.3. 550≤ T ≤ 900 °C

Figure 12 shows Raman (b) and FT-IR (b) spectra for heat treated powders in the 550 – 900 °C range. Unlike the previously studied temperature range, vibrational spectra did not show drastic or very noticeable changes. The FT-IR spectra features the only IR active band for aPZT-R3m in the 400-1500 cm^{-1} range (A1(3TO)); this band, associated to the extensional vibrations of the Perovskite BO_6 octahedra, shifts slightly to higher frequencies while gets narrower as temperature increases. This shifting suggests a more compact octahedral structure while a narrower band could be the evidence of a better 'environment' around the octahedron or, in other words, a better local stoichiometry [44] that seems to be minimum for T = 800°C, an indicative of an optimum crystallization. Raman spectra featured vibrational modes that tend to define better as temperature increases.

http://dx.doi.org/10.5772/51996

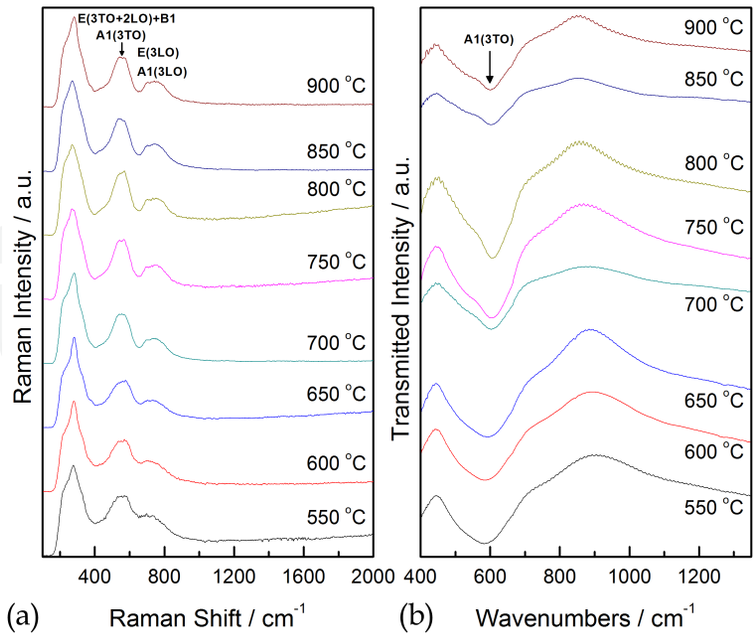

Figure 12. Phase transformations for 550 °C≤ T≤ 900 °C as registered by Raman (a) and FT-IR (b) vibrational spectroscopies.

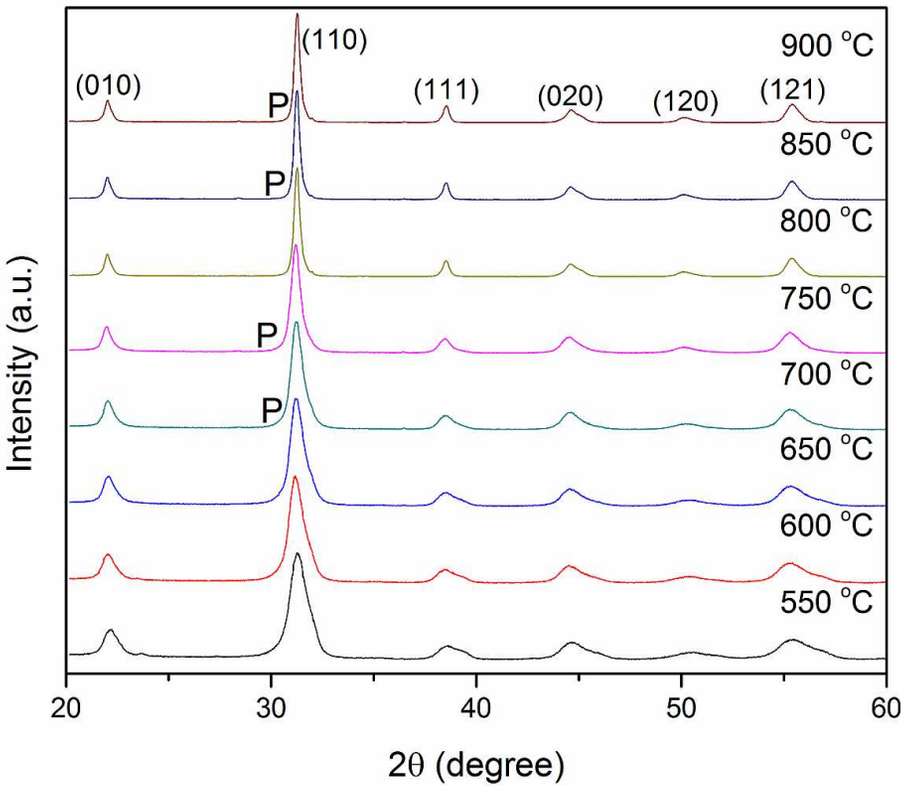

Figure 13. Thermal evolution of the powders under study when 550 °C ≤ T ≤ 900 °C as evidenced by XRD patterns in the 20 - 60 deg. 2θ interval. Regions where the most intense Pyr peak showed up are denoted by P.

XRD patterns depicted in Figure 13 allow us to notice the temperature evolution of the distinctive Perovskite diffraction peaks. Peaks indexing has been done according to a PZT 53/47, $F_{R(HT)}$; sym: R3m. Besides, regions where the most intense Pyr peak showed up (~28.5°) are denoted by P; the Pyr phase is present in a small percentage (%Pyr ~ 1 %) except for powders treated at T = 800°C which must be chosen as the appropriate crystallization temperature for this material. The final Perovskite phase homogenizes and tends to be predominant as temperature increases until lead losses become noticeable.

The rest of the PZT compositions that were chosen for this study, PZT (1-x)/x with C = 0.35 M and 2 months aged, were also treated at 800 °C in order to obtain the appropiate Perovskite phase; Figure 14 shows the corresponding XRD patterns for each one of them. As seen in the graph, all samples attained a perfect crystallization in the corresponding phase and the proper pattern indexing as well as the phase indentification are also shown.

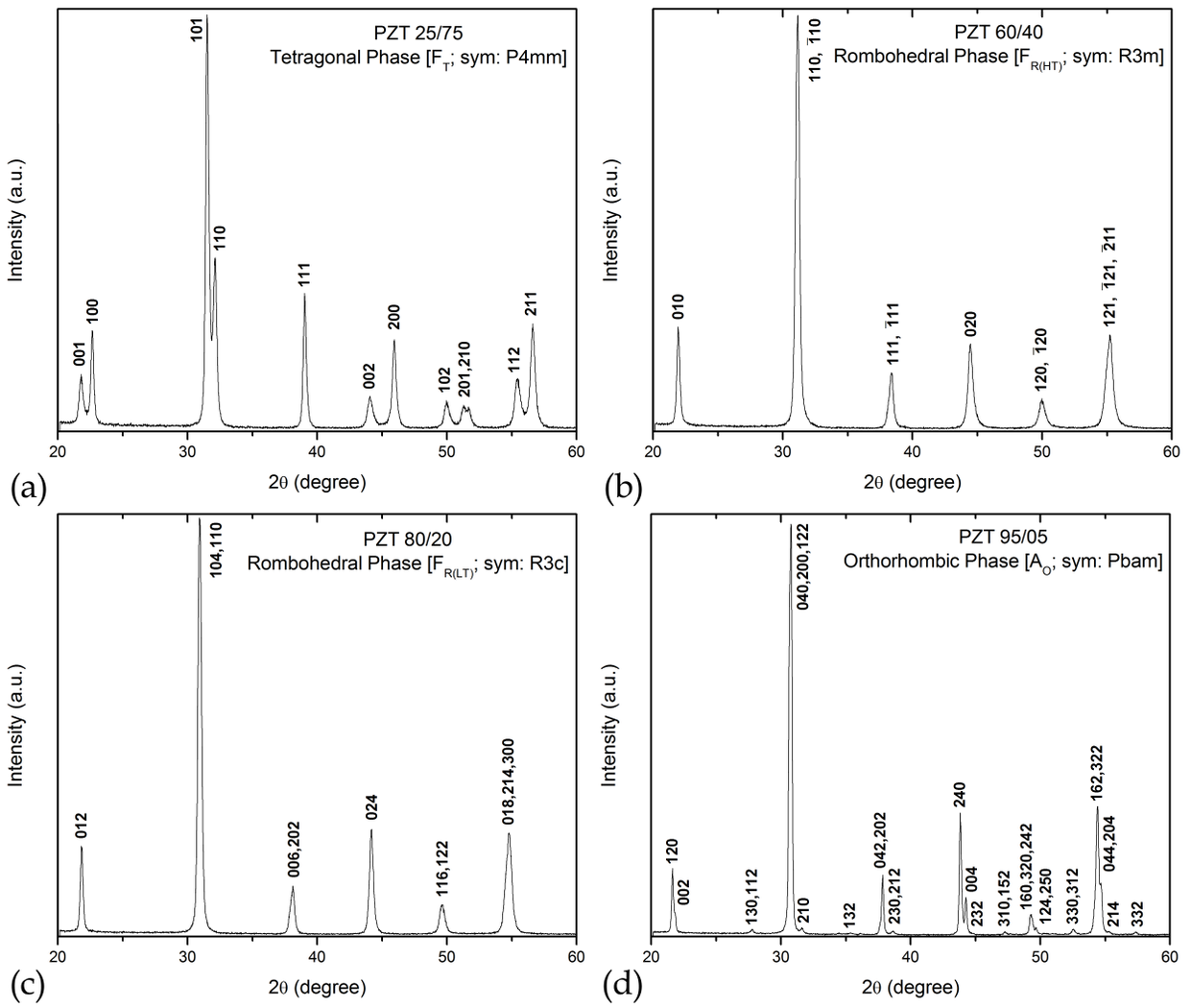

Figure 14. XRD patterns for PZT (1-x)/x under study: (a) PZT 25/75, (b) PZT 60/40, (c) PZT 80/20 and (d) PZT 95/05.

http://dx.doi.org/10.5772/51996

On the other hand, Figure 15 shows SEM micrographs of crystallized PZT (1-x)/x powdered samples. As illustrated, a granular structure of fair morphological uniformity is found in all cases along with a remarkable submicrometric average grain size. Another interesting feature is the low porosity found in all compositions, somehow resembling the granular structure of sintered bulk samples, which certainly favors the formation of a high density ferroelectric material.

As it was said at the beginning of this chapter, this kind of sub-micron granular structures, or nanoceramics, allows the technological exploitation of dielectric and ferro/piezoelectric size related features. It is not shown here, but that very same samples have been resynthesized a couple of times with starting reactants being bought to different companies and final results showed almost the same granular and morphological quality. Repetitiveness is also a bonus when working with chemical routes of synthesis that tend to be less straightforward, even though cheaper, than physical ones.

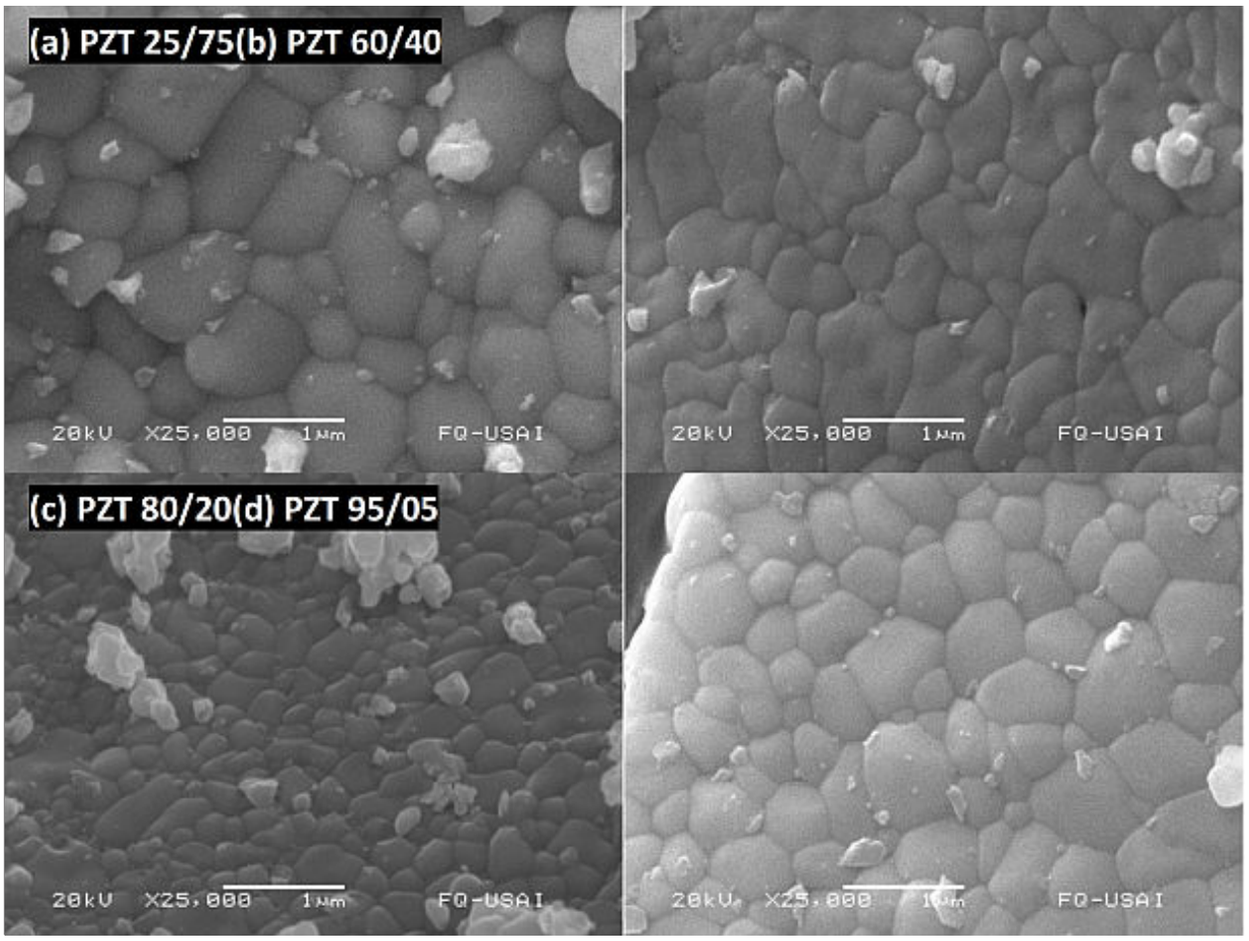

Figure 15. SEM micrographs showing the morphological quality of the PZT (1-x)/x powders when crystallized at 800 °C: (a) PZT 25/75, (b) PZT 60/40, (c) PZT 80/20 and (d) PZT 95/05.

5. Chapter remarks

Through this chapter, we tried to expose some relevant results directly concerned with a feasible 'universal' controlled synthesis of nano/submicrometric grain-sized PZT (1-x)/x piezoelectric structures that, technically speaking, potentially enhance the performance of current commercially bulk based devices by exploiting the size effects related phenomena that arise, as is commonly accepted, for grain sizes below 1 μm. Under the light of this study, the tentative bottom-up "design" of any desired nano/submicrometric PZT (1-x)/x structure seems to be a plausible and successful task that, methodologically at least, could be expanded to more complex materials systems.

Further reading regarding the work that has been shown here can be found in references [45]-[48]. On the other hand, references [49]-[60] will also provide the reader with very recent research papers in this field that undoubtedly extend the applicability and versatility of what has been discussed.

Author details

A. Suárez-Gómez[1], J.M. Saniger-Blesa[2] and F. Calderón-Piñar[3]

1 UdG-CUVALLES, Carr. Guadalajara-Ameca, Ameca, Jalisco, México

2 CCADET-UNAM, Cd. Universitaria, Coyoacán, México D.F., México

3 Fac. de Física/IMRE, San Lázaro y L, Univ. de la Habana, Habana , Cuba

References

[1] McCauley D, Newnham RE, Randall CA. Intrinsic size effects in a barium titanate glass-ceramic. Journal of the American Ceramic Society1998;81(4)979-987.

[2] Frey MH, Xu Z, Han P, Payne DA. The role of interfaces on an apparent grain size effect on the dielectric properties for ferroelectric barium titanate ceramics. Ferroelectrics1998;206(1)337-353.

[3] Zhang L, Zhong LW, Wang CL, Zhang PL, Wang YG. Finite-size effects in ferroelectric solid solution $Ba_xSr_{1-x}TiO_3$. Journal of Physics D: Applied Physics 1999;32 546-551.

[4] Park Y, Knowles KM, Cho K. Particle-size effect on the ferroelectric phase transition in $PbSc_{1/2}Ta_{1/2}O_3$ ceramics. Journal of Applied Physics 1998;83(11)5702-5708.

[5] Desu S.B., Ramesh R., Tuttle B.A., Jones R.E., Yoo I.K., editors. Ferroelectric Thin Films V (MRS Symposium Proceedings Series Vol. 433), San Francisco, CA, 1996.

[6] Wang ZL. The new field of nanopiezotronics. Materials Today 2007;10(5) 20-28.

[7] Budd K.D., Dey S.K., Payne DA. Sol-Gel Processing of $PbTiO_3$-$PbZrO_3$ and PLZT Thin Films. Proceedings of the British Ceramic Society 1985;36107–121.

[8] Schneller T, Waser R. Chemical Solution Deposition of Ferroelectric Thin Films: State of the Art and Recent Trends. Ferroelectrics 2002;267(1) 293–301.

[9] Majumder SB, Bhaskar S, Katiyar RS. Critical issues in sol-gel derived ferroelectric thin films: A review. Integrated Ferroelectrics 2002:42(1)245–292.

[10] Besra L, Liu M. A review on fundamentals and applications of electrophoretic deposition (EPD). Progress in Materials Science 2007;52(1) 1-61.

[11] Shantha Shankar K, Raychaudhuri AK. Fabrication of nanowires of multicomponent oxides: Review of recent advances. Materials Science and Engineering: C 2005;25(5–8) 738-751.

[12] Ogihara T, Kaneko H, Mizutani N, Kato M. Preparation of monodispersed lead zirconate-titanate fine particles. Journal of Materials Science Letters 1988;7(8) 867-869.

[13] Lakeman CDE, Payne DA. Processing Effects in the Sol–Gel Preparation of PZT Dried Gels, Powders, and Ferroelectric Thin Layers. Journal of the American Ceramic Society 1992;75(11) 3091-3096.

[14] Wang FP, Yu YJ, Jiang ZH, Zhao LC. Synthesis of $Pb_{1-x}Eu_x(Zr_{0.52}Ti_{0.48})O_3$ nanopowders by a modified sol–gel process using zirconium oxynitrate source. Materials Chemistry and Physics 2003;77(1)10-13.

[15] Brunckova H, Medvecky L, Briancin J, Saksi K. Influence of hydrolysis conditions of the acetate sol–gel process on the stoichiometry of PZT powders. Ceramics International 2004;30(3) 453-460.

[16] Praveenkumar B, Sreenivasalu G, Kumar HH, Kharat DK, Balasubramanian M,Murty BS. Size effect studies on nanocrystalline $Pb(Zr_{0.53}Ti_{0.47})O_3$ synthesized by mechanical activation route. Materials Chemistry and Physics 2009;117(2–3) 338-342.

[17] Livage J, Henry M, Sanchez C. Sol-gel chemistry of transition metal oxides. Progress in Solid State Chemistry 1988;18(4)259–342.

[18] Sedlar M, Sayer M. Reactivity of titanium isopropoxide, zirconium propoxide and niobium ethoxide in the system of 2-Methoxyethanol, 2,4-Pentanedione and water. Journal of Sol–Gel Science and Technology 1995;5(1) 27–40.

[19] Nakamoto K. Infrared and Raman Spectra of Inorganic and CoordinationCompounds. John Wiley & Sons; 1997.

[20] Doeuff S, Henry M, Sanchez C, Livage J. Hydrolisis of titanium alkoxides: Modification of the molecular precursor by acetic acid. Journal of Non-Crystalline Solids 1987;89(1-2) 206–216.

[21] Lewandowski H, Koglin E, Meier RJ. Computational study of the infrared spectrum of acetic acid, its cyclic dimer, and its methyl ester. Vibrational Spectroscopy 2005;39(1) 15–22.

[22] Yang MM, Crerar DA, Irish DE. A Raman spectroscopic study of lead and zinc acetate complexes in hydrothermal solutions. Geochimica et Cosmochimica Acta 1989;53(2) 319–326.

[23] Tayyari SF, Milani-nejad F. Vibrational assignment of acetylacetone. Spectrochimica Acta A: Molecular and Biomolecular Spectroscopy2000;56(14) 2679–2691.

[24] Schubert U, Husing N, Lorenz A. Hybrid Inorganic-Organic Materials by Sol-Gel Processing of Organofunctional Metal Alkoxides. Chemistry of Materials 7(11) 2010–2027.

[25] Accelrys Inc., San Diego, CA USA. http://accelrys.com/products/materials-studio/

[26] Schwartz RW, Voigt JA, Boyle TJ, Christenson TA, Buchheit CD,"Control of Thin Film Processing Behavior Through Precursor Structural Modifications. Ceramic Engineering and Science Proceedings 1995;16(5)1045–1056.

[27] Kolb U, Gutwerk D, Beudert R, Bertagnolli H. An IR- and EXAFS-study of the precursor system lead(II) acetate trihydrate, dissolved in methanol and 2-methoxyethanol. Journal of Non-Crystalline Solids 1997;217(2-3) 162-166.

[28] Zeisgerber M, Dutz S, Lehnert J, Müller R. Measurement of the distribution parameters of size and magnetic properties of magnetic nanoparticles for medical applications. Journal of Physics: Conference Series 2009;149(1) 012115.

[29] Ortega D, Garitaondia JS, Ramírez-del-Solar M, Barrera-Solano C, Domínguez M. Implications of nanoparticle concentration and size distribution in the superparamagnetic behaviour of aging-improved maghemite xerogels. The European Physics Journal D: Atomic, Molecular, Optical and Plasma Physics 2009;52(1-3) 19-22.

[30] Maity D, Choo SG, Yi J, Ding J, Xue JM. Synthesis of magnetite nanoparticles via a solvent-free thermal decomposition route. Journal of Magnetism and Magnetic Materials 2009;321(9) 1256-1259.

[31] Brinker CJ, Scherer GW. Sol–gel Science: The Physics and Chemistry of Sol–gel Processing. Academic Press Inc., San Diego; 1990.

[32] Das B, Hazra DK. Conductance of selected Alkali Metal Salts in Aqueous Binary Mixtures of 2-Methoxyethanol at 25 °C. Journal of Solution Chemistry 1998;27(11) 1021-1031.

[33] Valdés-Solís T, Marbán G, Fuertes AB. Preparation of Nanosized Perovskites and Spinels through a Silica Xerogel Template Route. Chemistry of Materials 2005;17(8) 1919-1922.

[34] Steinhart M, Jia Z, Schaper AK, Wehrspohn RB, Gösele U, Wendorff JH. Palladium Nanotubes with Tailored Wall Morphologies. Advanced Materials 2003;15(9) 706-709.

[35] Limmer SJ, Hubler TL, Cao G. Nanorods of Various Oxides and Hierarchically Structured Mesoporous Silica by Sol-Gel Electrophoresis. Journal of Sol–Gel Science and Technology 2003;26(1-3) 577-581.

[36] Urban JJ, Yun WS, Gu Q, Park H. Synthesis of Single-Crystalline Perovskite Nanorods Composed of Barium Titanate and Strontium Titanate. Journal of the American Chemical Society 2002;124(7) 1186-1187.

[37] Hardy A, Van Werde K, Vanhoyland G, Van Bael MK, Mullens J, Van Poucke LC. Study of the decomposition of an aqueous metal–chelate gel precursor for $(Bi,La)_4Ti_3O_{12}$ by means of TGA–FTIR, TGA–MS and HT-DRIFT. Thermochimica Acta 2003;397(1-2)143-153.

[38] Petzelt J, Ostapchuk T. Infrared and Raman spectroscopy of some ferroelectric perovskite films and ceramics. Journal of Optoelectronics and Advanced Materials 2003;5(3) 725-733.

[39] Meng JF, Katiyar RS, Zou GT, Wang XH. Raman Phonon Modes and Ferroelectric Phase Transitions in Nanocrystalline Lead Zirconate Titanate. Physica Status Solidi A: Applications and Materials Science 1997;164(2)851-862.

[40] Burns G, Scott BA. Raman Spectra of Polycrystalline Solids; Application to the $PbTi_{1-x}Zr_xO_3$ System. Physical Review Letters 1970;25(17) 1191-1194.

[41] Camargo ER, Leite ER, Longo E. Synthesis and characterization of lead zirconate titanate powders obtained by the oxidant peroxo method. Journal of Alloys and Compounds 2009;469(1-2)523-528.

[42] Wilkinson AP, Speck JS, Cheetham AK, Natarajan S, Thomas JM. In Situ X-ray Diffraction Study of Crystallization Kinetics in $PbZr_{1-x}Ti_xO_3$ (PZT, x = 0.0, 0.55, 1.0). Chemistry of Materials 1994;6(6)750-754.

[43] Kwok CK, Desu SB. Pyrochlore to perovskite phase transformation in sol-gel derived lead-zirconate-titanate thin films. Applied Physics Letters 1992;60(12)1430-1432.

[44] Lakeman CDE, Xu Z, Payne DA. Rapid Thermal Processing of Sol-Gel Derived PZT 53/47 Thin Layers. Proceedings of the Ninth IEEE International Symposium onApplications of Ferroelectrics, 1994. ISAF '94. 1995404-407.

[45] Suárez-Gómez A, Sato-Berrú R, Toscano RA, Saniger-Blesa JM, Calderón-Piñar F. On the synthesis and crystallization process of nanocrystalline PZT powders obtained by a hybrid sol–gel alkoxides route. Journal of Alloys and Compounds 2008;450(1-2) 380-386.

[46] Suárez-Gómez A, Saniger-Blesa JM, Calderón-Piñar F. The effects of aging and concentration on some interesting Sol-gel parameters: A feasibility study for PZT nano-

particles insertion on in-house prepared PAA matrices via electrophoresis. Journal of Electroceramics 2009;22(1-3) 136-144.

[47] Suárez-Gómez A, Saniger-Blesa JM, Calderón-Piñar F. A study on the stability of a PZT precursor solution based on the time evolutionof mean particles size and pH. Materials Chemistry and Physics 2010;123(1) 304-308.

[48] Suárez-Gómez A, Saniger-Blesa JM, Calderón-Piñar F. A Crystallization Study of Nanocrystalline PZT 53/47 Granular Arrays Using a Sol-Gel Based Precursor. Journal of Materials Science & Technology 2011;27(6) 489-496.

[49] Meng Q, Zhu K, Pang X, Qiu J, Shao B, Ji H. Sol-hydrothermal synthesis and characterization of lead zirconate titanate fine particles. Advanced Powder Technology 2012;In Press DOI:10.1016/j.apt.2012.06.004.

[50] Chiolerio A, Quaglio M, Lamberti A, Celegato F, Balma D, Allia P. Magnetoelastic coupling in multilayered ferroelectric/ferromagnetic thin films: A quantitative evaluation. Applied Surface Science 2012;258(20) 8072–8077.

[51] Bastani Y, Bassiri-Gharb N. Enhanced dielectric and piezoelectric response in PZT superlattice-like films by leveraging spontaneous Zr/Ti gradient formation. Acta Materialia 2012;60(3) 1346–1352.

[52] Stawski TM, Besselink R, Veldhuis SA, Castricum HL, Blank DHA, ten Elshof JE. Time-resolved small angle X-ray scattering study of sol–gel precursor solutions of lead zirconate titanate and zirconia. Journal of Colloid and Interface Science 2012;369(1) 184–192.

[53] Goel P, Vijayan N, Biradar AM. Complex impedance studies of low temperature synthesized fine grain PZT/CeO_2 nanocomposites. Ceramics International 2012;38(4) 3047–3055.

[54] Yin Y, Ye H, Zhan W, Hong L, Ma H, Xu J. Preparation and characterization of unimorph actuators based on piezoelectric $Pb(Zr_{0.52}Ti_{0.48})O_3$ materials. Sensors and Actuators A: Physical 2011;171(2) 332–339.

[55] Sachdeva A, Tandon RP. Effect of sol composition on dielectric and ferroelectric properties of PZT composite films. Ceramics International 2012;38(2) 1331–1339.

[56] Bochenek D, Skulski R, Wawrzała P, Brzezińska D. Dielectric and ferroelectric properties and electric conductivity of sol–gel derived PBZT ceramics. Journal of Alloys and Compounds 2011;509(17) 5356–5363.

[57] Chen W, Zhu W, Chen XF, Sun LL. Preparation of $(Ni_{0.5}Zn_{0.5})Fe_2O_4/Pb(Zr_{0.53}Ti_{0.47})O_3$ thick films and their magnetic and ferroelectric properties. Materials Chemistry and Physics 2011;127(1–2) 70–73.

[58] Zhong C, Wang X, Li L. Fabrication and characterization of high curie temperature $BiSc_{1/2}Fe_{1/2}O_3$–$PbTiO_3$ piezoelectric films by a sol–gel process. Ceramics International 2012;38(S1) S237–S240.

[59] Fuentes-Fernandez E, Baldenegro-Perez L, Quevedo-Lopez M, Gnade B, Hande A, Shah P, Alshareef HN. Optimization of $Pb(Zr_{0.53},Ti_{0.47})O_3$ films for micropower generation using integrated cantilevers. Solid-State Electronics 2011;63(1) 89–93.

[60] Kim SH, Koo CY, Lee J, Jiang W, Kingon AI. Enhanced dielectric and piezoelectric properties of low-temperature processed $Pb(Zr,Ti)O_3$ thick films prepared by hybrid deposition technique with chemical solution infiltration process. Materials Letters 2011;65(19–20) 3041–3043.

IntechOpen